Chinese Chemical Letters 37 (2026) 111391

Contents lists available at ScienceDirect

Chinese Chemical Letters

journal homepage: www.elsevier.com/locate/cclet

# Efficient charge separation by $Ti_3C_2$ MXene modified nano MIL-125(Ti) Schottky photocatalysts for $N_2$ reduction and tetracycline hydrochloride removal

Yangyang Sun[a,1], Tianyu Huang[a,1], Houqiang Ji[a], Tian Tian[a], Xingwang Zhu[a], Wenlin Xu[a], Huan Pang[a,b,*]

[a] School of Chemistry and Chemical Engineering (Institute for Innovative Materials and Energy), Yangzhou University, Yangzhou 225009, China
[b] State Key Laboratory of Coordination Chemistry, Nanjing University, Nanjing 210023, China

ARTICLE INFO

*Article history:*
Received 22 February 2025
Revised 18 April 2025
Accepted 28 May 2025
Available online 28 May 2025

*Keywords:*
MIL-125
MXene
Schottky photocatalysts
Photocatalytic $N_2$ reduction
Photocatalytic TCH degradation

ABSTRACT

In this study, we successfully construct a non-noble metal-based Schottky photocatalyst MX@MIL-125 (MX is shorted for $Ti_3C_2$ MXene) by combining the Ti-based metal-organic framework MIL-125(Ti) with $Ti_3C_2$ MXene. Leveraging the unique surface properties of MXene, a close and uniform distribution of nano-cake-like MIL-125(Ti) was achieved on the two-dimensional $Ti_3C_2$ MXene layers. The introduction of $Ti_3C_2$ MXene not only broadens the light absorption range but also adjusts the local coordination structure between the interfaces. This heterojunction significantly promotes the separation and transfer of photogenerated carriers. The photocatalytic $N_2$ reduction efficiency of MX@MIL-125-20 is 11-fold higher than that of pristine MIL-125(Ti) (48.8 *vs.* 4.6 μmol $g_{cat}^{-1}$ $h^{-1}$), and the photodegradation efficiency of tetracycline hydrochloride (TCH) is increased by about 18 % (92.95 % *vs.* 74.67 %). This work may provide new insights for the design of innovative photocatalysts for various chemical redox reactions.

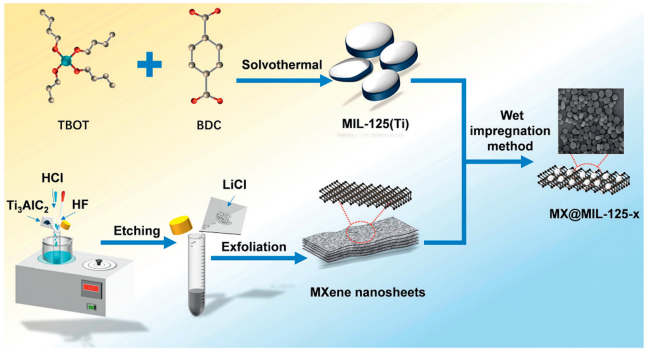
© 2025 Published by Elsevier B.V. on behalf of Chinese Chemical Society and Institute of Materia Medica, Chinese Academy of Medical Sciences.

Metal-organic frameworks (MOFs) are a class of porous inorganic-organic hybrid materials, which have broad application prospects in the fields of environment, industry, and energy [1–5]. Their ordered structure, high surface area, abundant active sites, and structural flexibility make them effective and potential candidates for the development of efficient and stable photocatalytic systems [6–8]. Titanium-based MOFs represented by MIL-125-(Ti) have become a research hotspot due to their structure tunability and surface functionality. MIL-125(Ti) consists of metal clusters and terephthalate linkers, which serves as photon-capturing antennas [9]. By adjusting synthetic conditions, the pore structure and chemical properties can be effectively altered to optimize catalytic performance [10,11]. However, MIL-125 as a photocatalyst face challenges, mainly including the short-wavelength light absorption in the UV region, fast charges recombination and slow separation of photocarriers, which leads to inefficiency performance of the photocatalytic reactions [12–14].

Constructing heterojunctions is one of the important strategies for separating electron-hole pairs in photocatalytic semiconductor materials [15,16]. This allows electrons and holes to be separated for a longer time, sufficient for reduction and oxidation reactions. It makes full use of the synergistic combination of various materials, which often have complementary properties. This combination leads to performance enhancement that exceeds individual components. In recent years, MXene, as an emerging two-dimensional (2D) transition metal layered structure, has attracted widespread attention in the field of catalysis due to its excellent metallic conductivity, unique surface properties, and good chemical stability [17–20]. Thus, MXene, represented by $Ti_3C_2T_x$, exhibit excellent catalytic performance. Among various heterostructures, heterostructures constructed by MXene and MOF materials have several significant advantages [21]. (1) Due to their atomically thin geometric thickness and relatively high surface area-to-volume ratio, they provide a large surface area-specific capacity. (2) The coverage of MOF materials enhances the chemical stability of MXenes, and maintains their inherent conductivity [22]. (3) The interfacial interactions in the heterostructures promote the redistribution of the electronic structure, thereby accelerating the redox reaction [23]. Therefore, constructing MXene-based

* Corresponding author.
*E-mail address:* panghuan@yzu.edu.cn (H. Pang).
[1] These authors contributed equally to the work.

https://doi.org/10.1016/j.cclet.2025.111391
1001-8417/© 2025 Published by Elsevier B.V. on behalf of Chinese Chemical Society and Institute of Materia Medica, Chinese Academy of Medical Sciences.




**Scheme 1.** Schematic diagram of the fabrication of MX@MIL-125-x composites. (nano MIL-125(Ti) TBOT: Tetrabutyl orthotitanate, BDC: benzene dicarboxylate).

MOF heterostructure is considered an effective way to improve photocatalytic reaction performance [24].

In this study, we have synthesized MX@MIL-125 Schottky heterostructure and further optimized the morphology of nano MIL-125 particles on the 2D MXene nanosheets. The optimized MX@MIL-125-20 with intimate interface has exhibited the best photocatalytic performance. By the introduction of MXene, MX@MIL-125 composites could exhibit the enhanced photocatalytic activity. Under visible light, MX@MIL-125-20 exhibits a photocatalytic nitrogen fixation of 48.8 μmol $g_{cat}^{-1}$ $h^{-1}$ *vs.* pure MIL-125(Ti) with 4.6 μmol $g_{cat}^{-1}$ $h^{-1}$, and the degradation efficiency of tetracycline hydrochloride is also increased by 18 %. The distinct fermi level of MXene and MIL-125(Ti) also effectively promotes charge transfer. It has been found that the electron transfers from the $Ti_3C_2$ MXene to MIL-125(Ti). Under illumination, MIL-125(Ti) is excited, and then photogenerated electrons will transfer from conduction band of MIL-125(Ti) to $Ti_3C_2$ MXene driven by built-in electric field. This study offers new insights for efficient $N_2$ conversion and advances photocatalytic wastewater treatment in support of sustainable development goals.

Nano MIL-125(Ti) was prepared by the assembly of TBOT and BDC organic linker by the solvothermal method. $Ti_3C_2$ MXene monolayers or a few layers were fabricated from acid etching of $Ti_3AlC_2$ bulk crystals and subsequent exfoliation of the accordion-like structure through LiCl intercalation, then the solid MXene was obtained from dry freezing. Finally, MX@MIL-125 composites were synthesized by wet impregnation method (Detail synthetic pathways of MIL-125(Ti), $Ti_3C_2$ MXene and MX@MIL-125 composites are shown in Supporting information). Nano MIL-125(Ti) with cake-like morphology were bonded onto the surface of the $Ti_3C_2$ MXene nanosheets by electrostatic interactions (Scheme 1) [25].

Scanning electron microscopy (SEM) and transmission electron microscopy (TEM) were adopted to characterize the morphology and structure of $Ti_3C_2$ MXene, MIL-125(Ti), and MX@MIL-125(Ti)-*x*. The morphology of as-synthesized $Ti_3C_2$ nanosheets (Fig. 1a) shows a lamellar structure with a rough surface. The MIL-125(Ti) in MX@MIL-125 composites exhibit regular cake-like morphology with a diameter of ≈500 nm and are homogeneously distributed on the $Ti_3C_2$ MXene nanosheets (Fig. 1b, Figs. S1 and S2 in Supporting information). For MX@MIL-125-2.5, -5, -10, the distribution ratio of $Ti_3C_2$ MXene in the composite is low and only a few MXene nanosheets can be observed (Fig. S1). For MX@MIL-125-20, MIL-125(Ti) was evenly and compactly distributed on the surface of the $T_3C_2$ MXene nanosheet with intimate contact, which is the optimized material for the photocatalytic application. With an increased amount of MXene, MX@MIL-125-40 shows that a few MIL-125(Ti) nanoparticles are sparsely distributed on the $T_3C_2$ MXene nanosheet, which is underutilized (Fig. S1). The different addition of MXene in the composites resulted in a change in the uniformity of the distribution of nano MIL-125(Ti) on the surface of MXene nanosheets. The energy-dispersive X-ray spectroscopy (EDS) analysis reveals the presence and uniform distribution of Ti, C, and O elements in MX@MIL-125-20, indicating the successful fabrication of MX@MIL-125 composites (Fig. 1c). MIL-125(Ti) is anchored on the MXene surface, which is conducive to electron transfer and surface catalytic reactions.

The crystal phase pattern and surface functional group of MX@MIL-125-*x* photocatalysts were in detail characterized. Comparing the X-ray diffraction (XRD) patterns of $Ti_3AlC_2$ and $Ti_3C_2$ MXene, the (002) peak of MXene shows a negative shift (Fig. S3 in Supporting information). This phenomenon indicates that the lattice expansion of $Ti_3C_2$ occurs under HF etching and intercalation of LiCl, resulting in a negative shift of the diffraction peak at low angles. The synthetized MIL-125(Ti) was consistent with the simulated, as shown in Fig. S4 (Supporting information). The XRD pattern (Fig. 1d) of MX@MIL-125-*x* exhibits similar characteristic diffraction peaks with MIL-125(Ti), suggesting that the crystalline structure of MIL-125(Ti) remained intact after being loaded onto 2D $Ti_3C_2$ MXene. Additionally, the peak at ~6.8 was ascribed to the (002) plane of $Ti_3C_2$ MXene, suggesting the coexistence of MIL-125(Ti) and $Ti_3C_2$ MXene. The crystal structure of the composite remains unchanged, but the intensity of the characteristic peaks is reduced due to the electrostatic interactions between MIL-125(Ti) and $Ti_3C_2$ MXene. In the Raman spectra (Fig. 1e), the signal peak of the composite material is roughly the same as that of MIL-125(Ti). The bands at 1611, 1448 and 1143 $cm^{-1}$ is attributed to the in-plane vibration mode of the benzene ring, whereas the peaks at 863 and 631 $cm^{-1}$ are assigned to out-of-plane vibration mode or C–H stretching of the benzene ring [26]. The addition of MXene did not change the structure of the composite, but with the increase of MXene content, the characteristic peak of MIL-125(Ti) gradually decreased. This indicates the interactions between $Ti_3C_2$ MXene and MIL-125(Ti). In the FT-IR spectra (Fig. 1f), the composite materials retain the same characteristic peaks as the initial MIL-125(Ti), including the characteristic peak of the carboxylate (O=C=O, C=O) at 1300–1600 $cm^{-1}$ and the stretching vibration (O–Ti–O) at the short wavelength (400–800 $cm^{-1}$) [27]. The Raman and FT-IR for $Ti_3C_2$ MXene were also measured (Fig. S5a and b in Supporting information) and the peaks assigned to $Ti_3C_2$ MXene in the composite was not obviously observed, due to the overlapping peak. The nitrogen adsorption-desorption isotherms and pore size distribution of MIL-125(Ti) and MX@MIL-125-20 shown in Fig. S6 (Supporting information). It shows that MIL-125(Ti) and MX@MIL-125-20 both have Type-I isotherms without hysteresis loops, which indicate the abundant micropores. The BET surface area of MIL-125(Ti) is 970.34 $m^2/g$ and MX@MIL-125-20 is slightly reduced to 931.97 $m^2/g$. Importantly, MX@MIL-125-20 composite still has a large BET surface and high porosity, which facilitates mass transfer, and provides support for rapid electron and hole transfer reactions [28].

To study the surface chemical states and the local electronic structure, the X-ray photoelectron spectroscopy (XPS) was processed. The XPS survey spectrum (Fig. 2a) of MIL-125(Ti), MX@MIL-125-20 and $Ti_3C_2$ MXene shows the existence of C, O, and Ti elements. As shown in Fig. 2b, the high-resolution Ti 2p spectrum in MIL-125(Ti) shows two main peaks at 458.65 and 464.58 eV, attributed to Ti $2p_{1/2}$ and Ti $2p_{3/2}$ orbitals of $Ti^{4+}$, and slight shoulder peaks at 457.32 and 463.27 eV, attributed to Ti $2p_{1/2}$ and Ti $2p_{3/2}$ orbitals of $Ti^{3+}$, respectively. For $Ti_3C_2$ MXene, the Ti 2p spectrum contains three sets of double peaks designated as Ti–C bond (454.56 and 460.32 eV), and Ti–O bond (457.79 and 462.84 eV for $Ti^{4+}$, 455.78 and 461.39 eV for $Ti^{3+}$) [29]. By hybridization MIL-125(Ti) with 2D $Ti_3C_2$ MXene, there are two sets of double peaks attributed to $Ti^{4+}$ (458.60 and 464.33 eV) and $Ti^{3+}$ (456.10 and 462.85 eV), and the double peaks of Ti–C bond (460.90 and

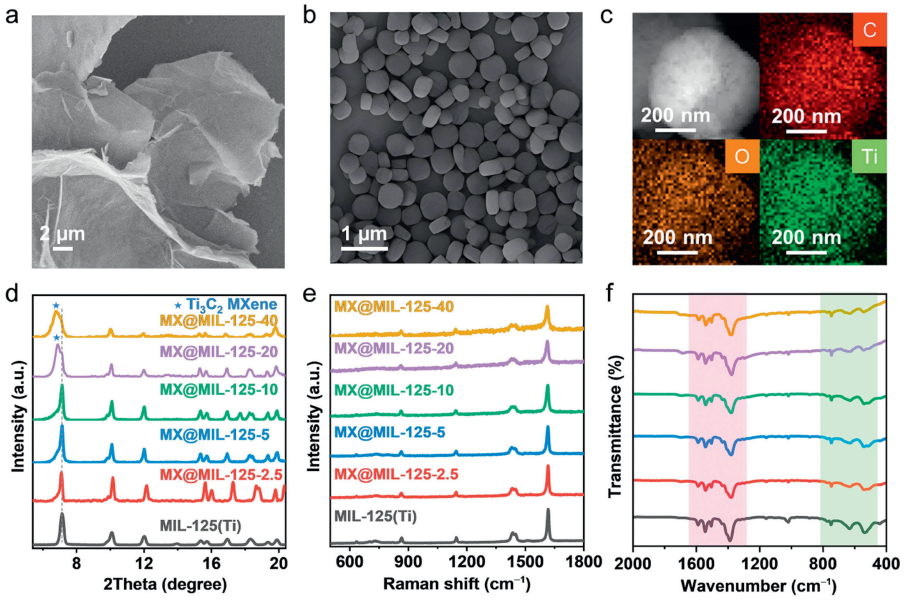



**Fig. 1.** The SEM images of (a) MXene and (b) MX@MIL-125-20, ($x = 2.5$, 5, 10, 20, 40). (c) The elemental mapping of MX@MIL-125-20, (d) Powder XRD pattern, (e) FTIR, and (f) Raman spectroscopy.

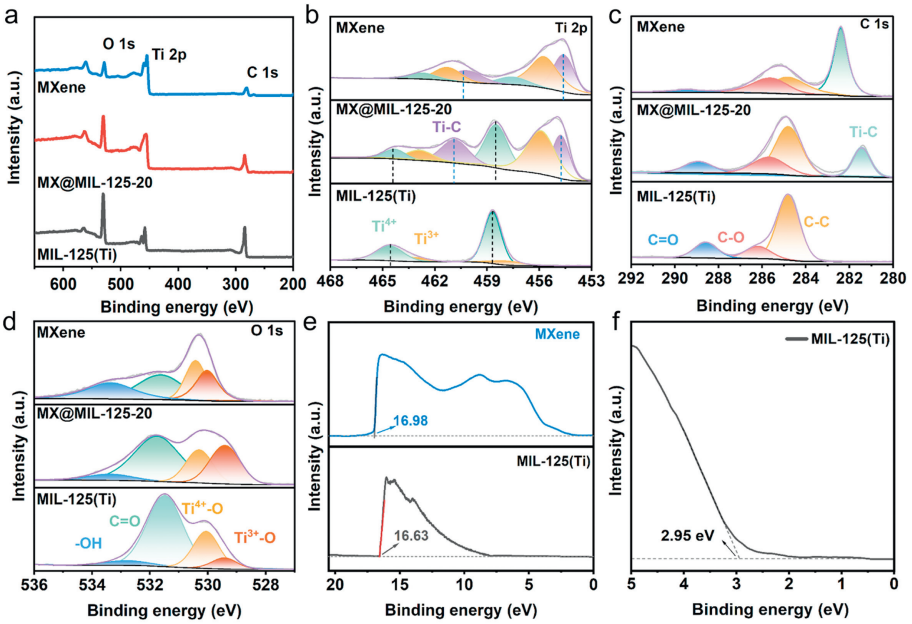



**Fig. 2.** XPS spectra of (a) full spectrum, high-resolution (b) Ti 2p, (c) C 1s, and (d) O 1s, (e) UPS spectrum of MIL-125(Ti) and $Ti_3C_2$ MXene and (f) valence band spectrum of MIL-125(Ti).

454.77 eV). Compared to MIL-125(Ti), the Ti peaks attributed to $Ti^{4+}$ and $Ti^{3+}$ in MX@MIL-125-20 shift to lower binding energy, while with the reference to $Ti_3C_2$ MXene, Ti peaks assigned Ti–C negatively shift to higher binding energy, indicating the electrons transfer from $Ti_3C_2$ MXene to MIL-125(Ti) in MX@MIL-125-20. In the C 1s spectrum of MIL-125(Ti) (Fig. 2c) shows three peaks at 284.80, 286.19, and 288.59 eV, attributed to C–C, C–O, and C=O, respectively [30]. For MX@MIL-125(Ti)-20, besides the above three peaks, an additional peak at 282.40 eV was observed, which can be assigned to C–Ti, similar to the peaks in $Ti_3C_2$ MXene [26]. The high-resolution O 1s XPS spectra (Fig. 2d) exhibited that four peaks were attributed to –OH, C=O, $Ti^{4+}$–O and $Ti^{3+}$–O respectively. Similarly, compared to MIL-125(Ti), the four peaks' positions in MX@MIL-125-20 are also shifted. The offset in binding energy indicates an interaction between MXene and MIL-125(Ti), and the transfer of electrons occurs at the MX@MIL125-20 interface. Additionally, the work function ($\Phi$) of MIL-125(Ti) and $Ti_3C_2$ MXene was measured using ultraviolet photoelectron spectroscopy (UPS) (Fig. 2e). The cutoff edge energies ($E_{cutoff}$) for MIL-125(Ti) and $Ti_3C_2$ MXene are 16.63 eV and 16.98 eV, respectively. By subtracting the cutoff edge energy ($E_{cutoff}$) from the photon energy (21.22 eV), the $\Phi$ values for MIL-125(Ti) and $Ti_3C_2$ MXene are calculated to be 4.59 and 4.24 eV, respectively [31,32]. Using the formula $\Phi = E_v - E_f$, where $E_v$ is the vacuum potential (0 eV), the Fermi energy levels for MIL-125(Ti) and $Ti_3C_2$ MXene are calculated to be −4.59 eV and −4.24 eV, respectively [33,34]. Thus, the electron transfers from the $Ti_3C_2$ MXene to MIL-125(Ti) when both materials come in contact [35,36]. The charge transfer induced by

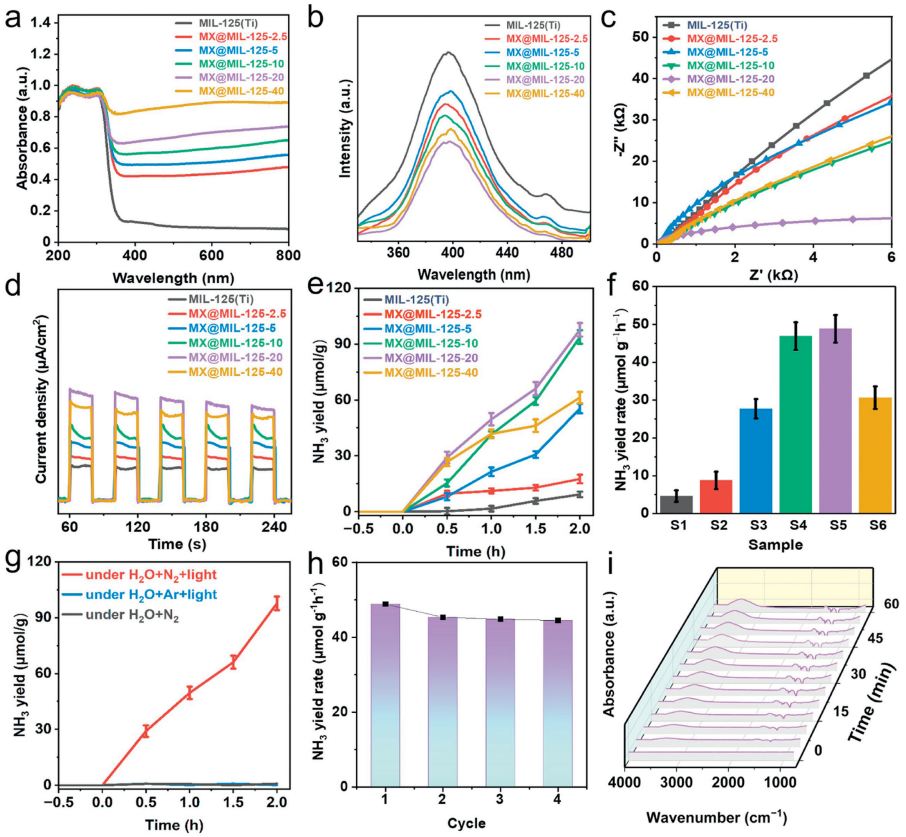



**Fig. 3.** (a) UV–vis DRS, (b) photoluminescence spectra, (c) electrochemical impedance spectra, (d) transient photocurrent response, (e) photocatalytic $NH_3$ evolution over time, (f) the $NH_3$ formation rate over MX@MIL-125-x samples, (g) control blank experiment, (h) cyclic experiments and (i) *in-situ* FT-IR.

the distinct Fermi energy levels of MIL-125(Ti) and $Ti_3C_2$ MXene also generates a space charge region, which induces the built-in electric field [37,38]. The valence band of MIL-125(Ti) is calculated to be 2.95 eV (XPS) from the UPS valence band spectrum (Fig. 2f). According to the formula $E_{VB}$ (*vs.* NHE) = $\Phi + E_{VB}$ (*vs.* NHE) - 4.44, where 4.44 refers to the conversion of vacuum level to electrode potential (pH 0), and the instrument's work function $\Phi$ is 4.2 eV, the value used for $E_{VB}$ (*vs.* NHE) is 2.71 eV, which is used for subsequent band analysis [39,40].

To analyze the light absorption abilities, UV–vis diffuse reflectance spectra (UV–vis DRS) of MX@MIL-125-*x* photocatalysts were employed (Fig. 3a). Compared to MIL-125(Ti), significantly enhanced absorption of MX@MIL-125 composites in the UV–visible regions were observed, due to the black MXene's strong absorption in the full spectrum. With the increase of the addition content of MXene, the absorption edge of the composites gradually took redshift and further shifted to the visible region. The phenomena indicates that the composites exhibit enhanced visible light absorption ability. The band gap values of MX@MIL-125 photocatalysts were determined according to the Kubelka–Munk equation. As shown in Fig. S7 (Supporting information), the $E_g$ value for MIL-125 (Ti) is 3.40 eV, while the band gaps are narrowed to be 3.06, 2.80, 2.88, 2.61, and 2.15 eV for MX@MIL-125-2.5, MX@MIL-125-5, MX@MIL-125-10, MX@MIL-125-20 and MX@MIL-125-40, respectively. To investigate the separation efficiency of photogenerated carriers, the photoluminescence (PL) spectra (Fig. 3b) of MIL-125(Ti) and MX@MIL-125 composites were conducted. MIL-125(Ti) has a strong emission peak at 396 nm, corresponding to a rapid recombination of photogenerated carriers. However, MX@MIL-125-20 shows the weakest PL intensity, which indicated the efficient suppression of the recombination of photogenerated carriers, and the superior photocarrier separation efficiency. From electrochemical impedance spectroscopy (EIS) curves (Fig. 3c), MX@MIL-125-20 has the smallest radius in all tested samples, indicating lowest charge transfer resistance. The transient photocurrent curves in Fig. 3d exhibited that MX@MIL-125-20 has the highest photocurrent responses among all the materials. Combined with PL, photocurrent, and ESI measurements, it can be concluded that the introduction of MXene as an electron transfer medium is very beneficial in promoting the separation of photogenerated electrons and holes [41].

The *p*-NRR performance of the catalysts was evaluated upon visible-light irradiation ($\lambda > 400$ nm) without a scavenger. Compared to the initial MIL-125(Ti), the photocatalytic nitrogen fixation performance of MX@MIL-125-*x* has significantly improved (Fig. 3e), due to the more favorable charge separation and transfer at the MXene@MIL-125 composite interface. The $N_2$ reduction rate (Fig. 3f) of MX@MIL-125-20 was approximately 11-fold higher than that of pristine (48.8 *vs.* 4.6 $\mu mol\, g_{cat}^{-1}\, h^{-1}$). With the increased amount of MXene, the photocatalytic performance gradually improved. However, excessive MXene into composites caused a decrease in $NH_3$ production rates, which is caused by the underutilization of the material due to the uneven distribution. The various MOF-based photocatalysts and their performance in the photocatalytic *p*NRR were summarized in Table S1. Considering the light conditions, the photocatalyst dosage, the volume of solution, the test method and other factors, the comparison cannot be accurately explained. Furthermore, to demonstrate the necessity of light irradiation and $N_2$, we conducted blank control experiments (Fig. 3g), in which the detected ammonia in the comparative experiments was negligible. The photocatalytic stability test of MX@MIL-125-20 is shown in Fig. 3h, where the ammonia yield remains essentially stable over four cycles. Moreover, MX@MIL-125-20 re-

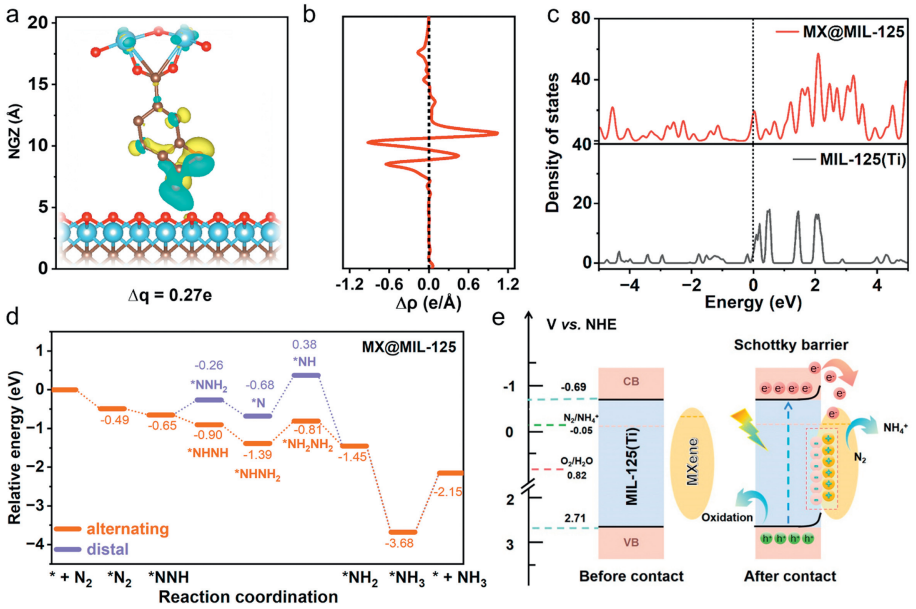



**Fig. 4.** (a) Calculated charge density difference of MX@MIL-125, where cyan and yellow areas indicate charge depletion and accumulation. (b) Plane charge density of $\Delta\rho(z)$ along the z axis, (c) density of states of Ti 3d orbital, (d) free energy calculation for $N_2$ reduction on MX@MIL-125. (e) Possible mechanism for photocatalytic reduction of $N_2$ to $NH_3$ upon MX@MIL-125.

mained crystal structure, and chemical composition based on powder XRD (PXRD), Raman, FTIR, and XPS (Figs. S8–S10 in Supporting information), however, SEM (Fig. S8) shows that the morphology of nano-cake-like MIL-125 in the composites occurred a small amount of damage.

To further explore the mechanism of the photocatalytic nitrogen reduction reaction, *in-situ* FTIR was used to track the reaction intermediates. As shown in Fig. 3i, a series of overlapping peaks appear near 3400 $cm^{-1}$ under irradiation, corresponding to the stretching vibrations of N–H/O–H [42]. The peak at 1644 $cm^{-1}$ is caused by the chemical adsorption of $N_2$ on the catalyst surface [43]. In addition, the two weak peaks at 1050 $cm^{-1}$ and 1373 $cm^{-1}$ are related to the stretching vibrations of N=N and N–N, further confirming the capture and activation of $N_2$ by MX@MIL-125-20 [44]. The bands at 1232 $cm^{-1}$ and 2935 $cm^{-1}$ correspond to the characteristic vibrations of $NH_4^+$ [45]. As the irradiation time increases, the intensity of these characteristic peaks increases, indicating the continuous occurrence of $N_2$ activation and conversion.

To gain a deep understanding of the interfacial interactions and electronic properties of MX@MIL-125, density functional theory (DFT) calculations were performed to determine the differential charge density (Fig. 4a). In the optimized configuration, the charge redistribution on MIL-125(Ti) surface is partially electron-accumulated, indicating that electron transfers from $Ti_3C_2$ MXene to MIL-125(Ti), which is consistent with the XPS and UPS experimental results. However, under the visible light, MIL-125(Ti) is excited, and then the photogenerated electrons at the conduction band (CB) of MIL-125(Ti) migrate to $Ti_3C_2$ MXene driven by the built-in electric field. Furthermore, Bader analysis reveals an electron transfer of 0.27e at the interlayer of the heterostructure. As shown in Fig. 4b, a significant charge transfer at the interface was also observed [46]. The density of states of the d-orbital (Fig. 4c) shows that the electronic density near the Fermi level in MX@MIL-125 is stronger than that in MIL-125, which is consistent with the smaller bandgap of MX@MIL-125 in Fig. S7. Energy diagrams of these two hydrogenation pathways for the reduction of $N_2$ to $NH_3$ are illustrated in Fig. 4d, and the adsorption energy of $N_2$ on MX@MIL-125 is −0.49 eV, smaller than the adsorption energy of −0.15 eV on MIL-125(Ti) (Figs. S11 and S12 in Supporting information). The rate-determining step for MX@MIL-125 is the last step from $^*NH_3$ to $NH_3$, with a barrier energy of 1.53 eV, indicating that both pathways can be carried out. As shown in Fig. 4e, a possible mechanism of catalytic reduction of $N_2$ to $NH_3$ upon MX@MIL-125 is proposed. Due to the lower $E_f$ level of MIL-125(Ti) than that of MXene, the electron transfers from the $Ti_3C_2$ MXene to MIL-125(Ti) when both materials come in contact. Under illumination, the photogenerated electrons in the conduction band of MIL-125 are transferred to MXene due to the built-in electric field. $Ti_3C_2$ MXene acted as an electron reservoir, allowing the photogenerated electrons to accumulate on its surface. Ti in MXene serves as an active site for $N_2$ adsorption. The interaction causes an energy band bending in MIL-125 and forms a Schottky barrier at the MX@MIL-125 interface, effectively inhibiting electron backflow. Thus, the formation of a Schottky heterojunction at the interface of MX@MIL-125 effectively promotes the charge separation and transfer, achieving effective photocatalytic reactions under visible light illumination.

Besides, we also studied the photocatalytic degradation of tetracycline hydrochloride (TCH). Without any catalyst, the self-degradation efficiency of TCH remains almost unchanged within 240 min, indicating that TCH has poor self-degradation ability under light [47]. The results in Fig. 5a show that MIL-125(Ti) degrades TCH with a degradation rate of 74.67 % within 120 min under visible light. After the introduction of MXene, MX@MIL-125-x shows a stronger response to visible light under the same conditions, and MX@MIL-125-20 exhibited the best among all the MX@MIL-125 samples, achieving a photocatalytic degradation capability of up to 92.95 %. Table S2 compares the photocatalytic degradation performance of MIL-125(Ti) and its modified materials. The performance of MX@MIL-125-20 is superior to that of other reported MIL-125(Ti)-based materials. To compare the degradation rate of different catalysts, the first-order kinetic model was adopted [48], and matched well with the experimental degradation results under visible light irradiation. From Fig. 5b, MX@MIL-125-20 has the best photocatalytic degradation rate constant, reaching 0.01934 $min^{-1}$.

To identify the predominant free radicals involved in the degradation of TCH by the photocatalyst, we performed the free radical capture experiments, respectively [49,50]. Three types of free

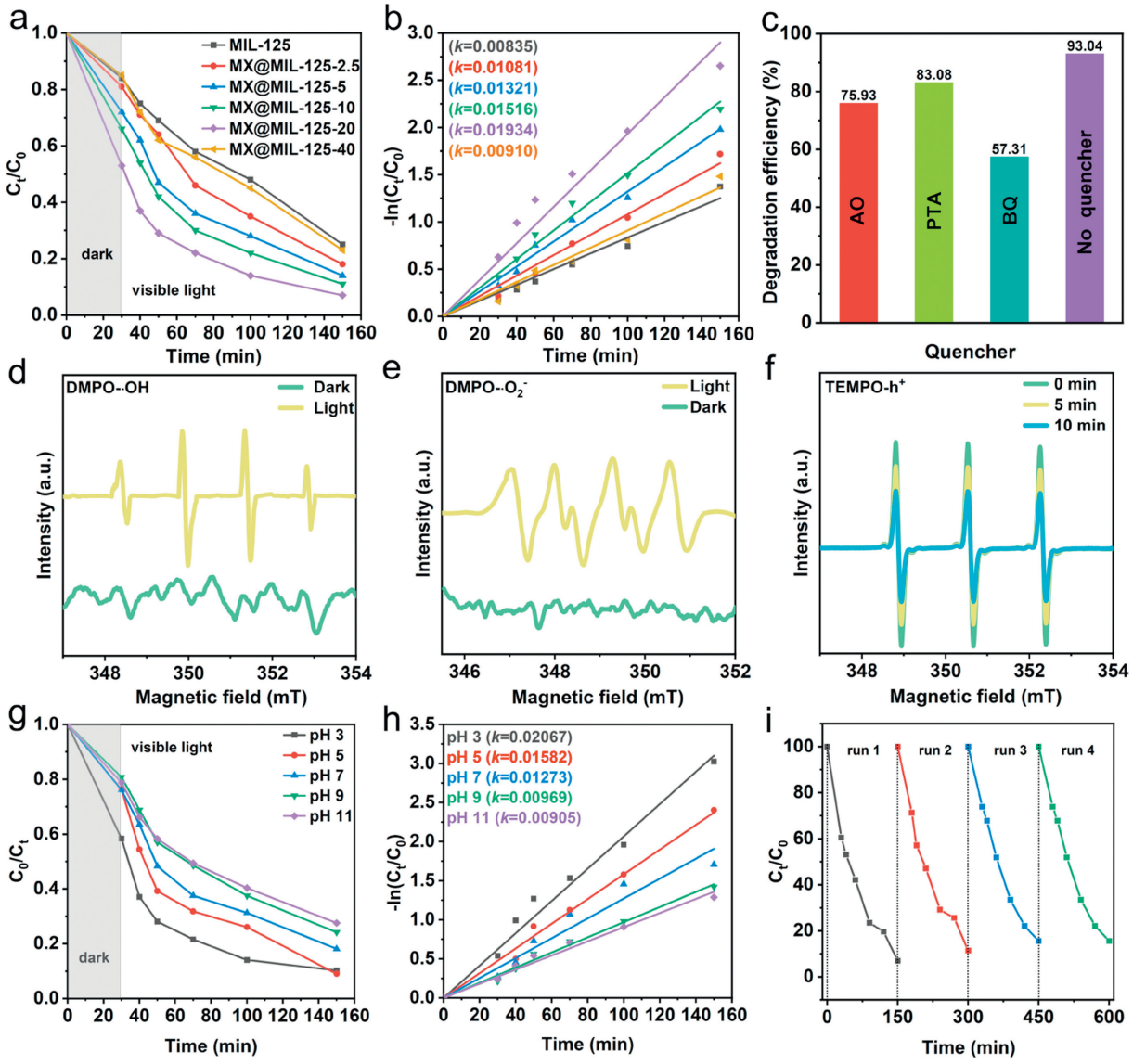



**Fig. 5.** (a) Photocatalytic degradation of TCH under visible light by MIL-125(Ti) and MX@MIL-125. (b) Linear fitting for *pseudo*-first-order kinetics. (c) Photocatalytic degradation of TCH by MX@MIL-125-20 with different quenchers. EPR spectra of MX@MIL-125 with DMPO (d) in DI water, in MeOH (e), and (f) TEMPO in DI solution. (g) Photocatalytic degradation of TCH by MX@MIL-125-20 at different pH levels. (h) *Pseudo*-first-order kinetics and rate constant (k) at different pH levels. (i) Recycling tests of MX@MIL-125-20.

radical quenchers, terephthalic acid (PTA), benzoquinone (BQ), and ammonium oxalate (OA) were adopted, which can capture ·OH, $\cdot O_2^-$, and $h^+$, respectively [51]. It was found that the apparent rate constant of photocatalytic degradation of TCH in the presence of each free radical quencher was reduced to different degrees (Fig. 5c). Notably, after capturing $\cdot O_2^-$ and $h^+$, the photocatalytic degradation efficiency of the MX@MIL-125-20 catalyst decreased significantly, from the original 92.95 % to 57.31 % and 75.93 %, respectively. It can be inferred that $\cdot O_2^-$ and $h^+$ are the main active radicals for photocatalytic TCH degradation. Overall, the contribution is in the order of $\cdot O_2^- > h^+ > \cdot OH$. Besides, the electron paramagnetic resonance (EPR) measurements (Fig. S13 in Supporting information) were carried out on MX@MIL-125-20, which further confirms the existence of the active species generated in the degradation process [52]. As shown in Figs. 5d and e, no obvious peaks are shown under the dark conditions. Under the visible light, the characteristic peaks of DMPO-·OH (1:2:2:1) and DMPO-$\cdot O_2^-$ (2:2:1:2:1:2) are observed. The signal of TEMPO-$h^+$ (1:1:1) in Fig. 5f decreases with the irradiation time, which indicates the generation of $h^+$ during the photodegradation process.

Based on the results of the radical control experiments, a possible reaction pathway for the photocatalytic degradation of TCH by MX@MIL-125-20 is proposed, as shown in the following reaction equations:

$$\text{MIL-125} + h\nu \rightarrow \text{MIL-125}\ (e_{CB}^- + h_{VB}^+) \rightarrow \text{MIL-125}\ (h_{VB}^+) + \text{MXene}\ (e_{CB}^-) \quad (1)$$

$$\text{MXene}\ (e_{CB}^-) + O_2 \rightarrow \cdot O_2^- \quad (2)$$

$$H_2O \Leftrightarrow H^+ + OH^- \quad (3)$$

$$\cdot O_2^- + 2H^+ \rightarrow 2\cdot OH \quad (4)$$

$$\text{MIL-125}\ (h_{VB}{}^{+}) + OH^{-} \rightarrow \cdot OH \quad (5)$$

$$\cdot O_2{}^{-}/h^{+}/\cdot OH + TCH \rightarrow \text{Degradation products} \quad (6)$$

Under the visible light irradiation, the electrons are transferred from the conduction band (CB) in MIL-125(Ti) to $Ti_3C_2$ MXene, and the adsorbed $O_2$ on the surface of material interacts with the electrons, and the $\cdot O_2{}^{-}$ is formed, which is the main active substance for degrading tetracycline [53]. In addition, ·OH is generated from the combination of $\cdot O_2{}^{-}$ with $H^{+}$ ($H_2O$) and the combination of $h^{+}$ in the value band (VB) in MIL-125(Ti) with $OH^{-}$ ($H_2O$) [54,55]. Thus, all three free radicals contribute to the photocatalytic degradation of TCH in the system [56,57]. In addition, the UV–vis absorption spectra of TCH degradation solutions at different reaction times were collected and analyzed (Fig. S13 in Supporting information). To further explore the dependence of MX@MIL-125 composite on pH, we studied the effect of pH on the photocatalytic TCH degradation by MX@MIL-125-20. Fig. 5g shows that the photocatalytic TCH degradation efficiency of MX@MIL-125-20 decreases with the increase of pH, demonstrating that an acidic environment is favorable for the photocatalytic reaction [58]. The morphology of MX@MIL-125-20 after photocatalytic TCH degradation at different pH is shown in Fig. S14 (Supporting information), which indicates that the structure is maintained under acidic and neutral conditions, but collapses under alkaline conditions. In addition, the photocatalytic degradation reaction rate at pH 3 is the fastest (Fig. 5h), reaching $0.02067 \times 10^{-2}\,L\,mg^{-1}\,min^{-1}$. In addition, we also conducted cycle experiments of degradation experiments on MX@MIL-125-20. It is shown in Fig. 5i that MX@MIL-125-20 still maintains good photocatalytic performance after four cycles. Therefore, MX@MIL-125-20 composite has good stability, which is a potential candidate for photocatalytic redox reactions.

In summary, we have designed a non-noble metal-based Schottky photocatalyst MX@MIL-125, where nano MIL-125(Ti) is closely and evenly distributed on the 2D $Ti_3C_2$ MXene layer. Due to the black body of $Ti_3C_2$ MXene, the light absorption range of MIL-125(Ti) is broadened, and thus the band gap is narrowed. Due to the distinct Fermi level, electron transfers from the $Ti_3C_2$ MXene to MIL-125(Ti) when both materials come in contact. Under the visible light, MIL-125(Ti) is photoexcited, and then photogenerated electrons will transfer from MIL-125(Ti) to $Ti_3C_2$ MXene driven by built-in electric field. Importantly, the formation of a Schottky barrier at the MX@MIL-125 interface effectively suppresses electron backflow and the recombination of photogenerated charge carriers, significantly promoting charge separation and transfer. MX@MIL-125-20 exhibits a photocatalytic nitrogen fixation of $48.8\,\mu mol\,g_{cat}{}^{-1}\,h^{-1}$, which is 11-fold higher than MIL-125(Ti) with $4.6\,\mu mol\,g_{cat}{}^{-1}\,h^{-1}$. Besides, MX@MIL-125-20 also performs an enhanced photocatalytic HTC degradation of about 18 %, compared to MIL-125(Ti). This study provides innovative insights into the design of MXene-based MOFs heterostructures for various chemical redox reactions.

## Declaration of competing interest

The authors declare that they have no known competing financial interests or personal relationships that could have appeared to influence the work reported in this paper.

## CRediT authorship contribution statement

**Yangyang Sun:** Writing – review & editing, Methodology, Conceptualization. **Tianyu Huang:** Writing – original draft, Investigation. **Houqiang Ji:** Investigation. **Tian Tian:** Supervision. **Xingwang Zhu:** Validation, Software. **Wenlin Xu:** Supervision. **Huan Pang:** Writing – review & editing, Supervision.

## Acknowledgments

This work was supported by the National Natural Science Foundation of China (No. 52371240). The Jiangsu Province Excellent Postdoctoral Program (No. 2022ZB613). We thank the State Key Laboratory of Coordination Chemistry for the project and technical support.

## Supplementary materials

Supplementary material associated with this article can be found, in the online version, at doi:10.1016/j.cclet.2025.111391.

## References

[1] X. Xu, Q. Wei, Z. Xi, et al., Coord. Chem. Rev. 495 (2023) 215393.
[2] Z. Liang, C. Qu, W. Guo, et al., Adv. Mater. 30 (2017) 1702891.
[3] K.A. Adegoke, A.K. Oyebamiji, A.O. Adeola, et al., Coord. Chem. Rev. 517 (2024) 215959.
[4] Y. Zhou, B. Niu, B. Wu, et al., Acta Pharm. Sin. B 10 (2020) 2404–2416.
[5] X. Zhao, X. Miao, Coord. Chem. Rev. 502 (2023) 215611.
[6] D. Li, M. Kassymova, X. Cai, et al., Coord. Chem. Rev. 412 (2020) 213262.
[7] Y.T. Zheng, S. Li, N.Y. Huang, et al., Coord. Chem. Rev. 510 (2024) 215858.
[8] T. Huang, H. Yang, W. Xu, et al., Chem. Catal. 4 (2024) 100929.
[9] Z. Yang, X. Xu, X. Liang, et al., Appl. Catal. B 205 (2016) 42–54.
[10] C. Liu, Q. Chen, Y. Chen, et al., J. Colloid Interface Sci. 678 (2024) 616–626.
[11] V. Likodimos, Appl. Catal. B 230 (2018) 269–303.
[12] R. Fatima, J.O. Kim, Appl. Surf. Sci. 541 (2021) 148503.
[13] Y. Sun, H. Ji, Y. Sun, et al., Angew. Chem. Int. Ed. 62 (2023) e202316973.
[14] R. Pietro, C. Luca, S. Luigi, et al., Appl. Catal. B 345 (2024) 123692.
[15] P.V. Hlophe, L.C. Mahlalela, L.N. Dlamini, Sci. Rep. 9 (2019) 10044.
[16] C. Liu, Y. Yu, X. Zhang, et al., J. Water Process. Eng. 69 (2025) 106857.
[17] H. Ji, Y. Liu, G. Du, et al., Chem. Res. Chin. Univ. 40 (2024) 943–963.
[18] A. Zhou, Y. Liu, S. Li, et al., J. Adv. Ceram. 10 (2021) 1194–1242.
[19] X. Xie, N. Zhang, Adv. Funct. Mater. 30 (2020) 2002528.
[20] T. Su, C. Men, L. Chen, et al., Adv. Sci. 9 (2021) 2103715.
[21] G. Zhang, H. Yang, H. Zhou, et al., Angew. Chem. Int. Ed. 63 (2024) e202401903.
[22] J. Liu, H.-B. Zhang, R. Sun, et al., Adv. Mater. 29 (2017) 1702367.
[23] X. Tao, Y. Gao, S. Wang, et al., Adv. Energy Mater. 9 (2019) 1803951.
[24] X. Qian, Y. Wei, M. Sun, et al., Chinese J. Catal. 43 (2022) 1937–1944.
[25] H. Wang, R. Zhao, J. Qin, et al., ACS Appl. Mater. Interfaces 11 (2019) 44249–44262.
[26] Z. Shen, F. Li, L. Guo, et al., Appl. Catal. B 346 (2024) 123732.
[27] Z. Liu, Y. Wu, J. Chen, et al., Catal. Sci. Technol. 8 (2018) 1936–1944.
[28] B. Zhang, J. Zhang, X. Tan, et al., ACS Appl. Mater. Interfaces 10 (2018) 16418–16423.
[29] Z. Wu, J. Shen, Z. Li, et al., ACS Nano 19 (2025) 1832.
[30] Z. Gao, J. Wang, Y. Muhammad, et al., Chem. Eng. J. 388 (2020) 124389.
[31] Y. Fan, X. Hao, N. Yi, et al., Appl. Catal. B 357 (2024) 124313.
[32] Y. Xi, Y. Xiang, T. Bao, et al., Angew. Chem. Int. Ed. 63 (2024) e202409163.
[33] Z. Liu, W. Gao, L. Liu, et al., J. Hazard. Mater. 442 (2022) 130036.
[34] Y. Wang, Z. Li, H. Zhu, et al., Chem. Eng. J. 484 (2024) 149583.
[35] X. An, W. Wang, J. Wang, et al., Phys. Chem. Chem. Phys. 20 (2018) 11405–11411.
[36] X. Yu, R. Du, B. Li, et al., Appl. Catal. B 182 (2015) 504–512.
[37] X. Ruan, X. Cui, Y. Cui, et al., Adv. Energy Mater. 12 (2022) 2200298.
[38] H. Lv, C. Zhou, Q. Shen, et al., J. Colloid Interface Sci. 677 (2024) 365–376.
[39] T. Bao, Y. Xi, C. Zhang, et al., Natl. Sci. Rev. 11 (2024) nwae093.
[40] J. Wang, Z. Wang, K. Dai, et al., J. Mater. Sci. Technol. 165 (2023) 187–218.
[41] K. Zhang, F. Chu, Y. Hu, et al., Chin. Chem. Lett. 34 (2022) 107766.
[42] J. Ye, J. Xu, C. Li, et al., J. Mater. Chem. A 9 (2021) 24600–24612.
[43] P. Li, Z. Zhou, Q. Wang, et al., J. Am. Chem. Soc. 142 (2020) 12430–12439.
[44] L. Xiong, Y. Hu, Y. Yang, et al., Appl. Catal. B 317 (2022) 121660.
[45] X. Dong, X. Shi, Z. Cui, et al., ACS Nano 18 (2024) 9670–9677.
[46] Y.J. Yuan, Z.K. Shen, S. Song, et al., ACS Catal. 9 (2019) 7801–7807.
[47] W. Jiang, Z. Li, C. Liu, et al., J. Alloys Compd. 854 (2021) 157166.
[48] Z. Liu, X. Yu, Y. Wei, et al., Environ. Res. 268 (2025) 120788.
[49] J. Tang, G. Gao, W. Luo, et al., Adv. Compos. Hybrid Mater. 6 (2023) 190.
[50] X. He, T. Kai, P. Ding, Environ. Chem. Lett. 19 (2021) 4563–4601.
[51] J. Chen, X. Zhang, F. Bi, et al., J. Colloid Interface Sci. 571 (2020) 275–284.
[52] J. Nie, X. Yu, Z. Liu, et al., J. Clean. Prod. 363 (2022) 132593.
[53] X. Yu, Y. Tian, Y. Wei, et al., J. Alloys Compd. 1005 (2024) 175998.
[54] Y. Wu, X. Li, Q. Yang, et al., Chem. Eng. J. 390 (2020) 124519.
[55] X. Song, J. He, Y. Wang, et al., J. Colloid Interface Sci. 645 (2023) 918–932.
[56] K. Gao, L.A. Hou, X. An, et al., Appl. Catal. B 323 (2022) 122150.
[57] J. Nie, X. Yu, Z. Liu, Appl. Surf. Sci. 576 (2022) 151842.
[58] J. Cui, X. Xu, L. Yang, et al., Chem. Eng. J. 395 (2020) 125174.